JGR Solid Earth

RESEARCH ARTICLE
10.1029/2023JB026718

Phase-Field Simulation of Texture Evolution in Magmatic Rocks

J. Kundin[1], I. Steinbach[1], and S. Chakraborty[2]

[1]Interdisciplinary Centre for Advanced Materials Simulation (ICAMS), Ruhr-University Bochum, Bochum, Germany, [2]Institut of Geology, Mineralogy and Geophysics, Ruhr-University Bochum, Bochum, Germany

Key Points:

- Phase-field modeling
- Crystal size distribution (CSD)
- Diffusion chronometry

Correspondence to:

J. Kundin,
julia.kundin@rub.de

Citation:

Kundin, J., Steinbach, I., & Chakraborty, S. (2023). Phase-field simulation of texture evolution in magmatic rocks. *Journal of Geophysical Research: Solid Earth*, *128*, e2023JB026718. https://doi.org/10.1029/2023JB026718

Received 16 MAR 2023
Accepted 14 MAY 2023

Author Contributions:

Conceptualization: J. Kundin, S. Chakraborty
Data curation: J. Kundin, S. Chakraborty
Formal analysis: J. Kundin, S. Chakraborty
Funding acquisition: J. Kundin
Investigation: J. Kundin
Methodology: J. Kundin, I. Steinbach, S. Chakraborty
Project Administration: J. Kundin, S. Chakraborty
Resources: I. Steinbach
Software: I. Steinbach
Validation: J. Kundin
Visualization: J. Kundin
Writing – original draft: J. Kundin, I. Steinbach, S. Chakraborty
Writing – review & editing: J. Kundin, I. Steinbach, S. Chakraborty

Abstract The tool of phase-field modeling for the prediction of chemical as well as microstructural evolution during crystallization from a melt in a mineralogical system has been developed in this work. We provide a compact theoretical background and introduce new aspects such as the treatment of anisotropic surface energies that are essential for modeling mineralogical systems. These are then applied to two simple model systems—the binary olivine-melt and plagioclase-melt systems - to illustrate the application of the developed tools. In one case crystallization is modeled at a constant temperature and undercooling while in the other the process of crystallization is tracked for a constant cooling rate. These two examples serve to illustrate the capabilities of the modeling tool. The results are analyzed in terms of crystal size distributions (CSD) and with a view toward applications in diffusion chronometry; future possibilities are discussed. The modeling results demonstrate that growth at constant rates may be expected only for limited extents of crystallization, that breaks in slopes of CSD-plots should be common, and that the lifetime of a given crystal of a phase is different from the lifetime of this phase in a magmatic system. The last aspect imposes an inherent limit to timescales that may be accessed by diffusion chronometry. Most significantly, this tool provides a bridge between CSD analysis and diffusion chronometry—two common tools that are used to study timescales of magmatic processes.

Plain Language Summary We have developed a phase field model for predicting both chemical and microstructural evolution during melt crystallization in a mineralogical system. Here we provide a theoretical background of how phase field models work and focus on some aspects that are necessary for modeling mineralogical systems with non-cubic crystals. The model is applied to two simple cases as illustrations—the binary olivine melt and plagioclase melt systems. In one case, crystallization is modeled at a constant temperature, while the other monitors the crystallization process at a constant cooling rate. The results are analyzed from the point of view of applications to study the time scales of magmatic processes using crystal size distribution and diffusion chronometry.

1. Introduction

Physical chemistry is used to quantify the reading of the rock record to decipher processes that took place in and on the Earth. Thermodynamic analysis of complex chemical systems that correspond to bulk chemistry of diverse igneous and metamorphic rock types is now commonplace. Such analyses predict the stable mineral assemblages as well as the modal abundance and composition of the minerals as a function of intensive thermodynamic variables such as pressure, temperature, and fugacities of various species (e.g., f_{O_2}, f_{H_2O}). Petrological attributes of the rock record also include textural and microstructural characteristics, but a quantitative thermodynamically consistent approach to handle that is not yet available.

The situation is analogous to kinetic analysis. Studies of processes such as diffusion, nucleation, or crystal growth address these processes in individual mineral systems, or populations of crystals in some cases (e.g., nucleation and growth in molten systems), but in a manner that is generally decoupled from quantitative thermodynamic phase relations. In the best of cases, modeling efforts include alternating updates of thermodynamic and kinetic parameters, but without a means of ensuring physico-chemical consistency between these. Previous models for the simulation of texture evolution during crystallization processes in rocks were stochastic approaches, which were developed to validate theoretical models of the crystal size distribution with constant growth rates and an exponential nucleation rate (Amenta, 2001, 2004; Amenta et al., 2007; Hersum & Marsh, 2006, 2007;

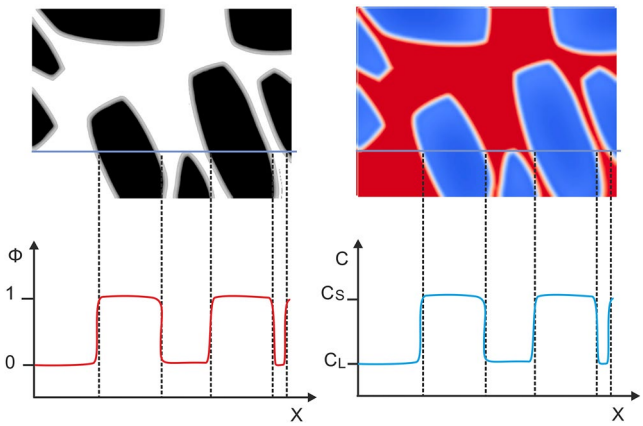

Figure 1. Scheme of a solidifying mush. The upper part shows (left) order parameter (solid in black, liquid in white) and (right) concentration field. Measuring the order parameter and the composition along the line scan gives the saw tooth thread profile as displayed in the lower part of the figure: (left) alternating between $\phi = 1$ in solid and $\phi = 0$ in liquid, (right) alternating between the composition in solid, c_S, and liquid, c_L.

Marsh, 1988; Spillar & Dolejs, 2015). However, these models do not take into account thermodynamic conditions and operate with artificially imposed growth rates.

The emerging tool of phase-field (PF) modeling and analysis provides a means of addressing these problems (Boettinger et al., 2002; Chen, 2002; Karma, 2001; Kundin & Steinbach, 2019; Kundin et al., 2015; Langer, 2021; Steinbach, 2009). Notably, the method couples the energetics of surfaces and interfaces with bulk thermodynamics, which is generally considered in the analysis of phase equilibria and diffusion. The minimization of overall free energy taking these aspects into account allows the calculation of not only the stable configurations of solids and liquids in terms of their chemistry, but also geometrical features such as grain size, shape, and distribution. Thus, commonly used tools such as crystal size distribution (CSD) may be placed on a more quantitative foundation than has been possible until now.

As a tool, the phase-field method has rarely been applied to mineralogical systems. Some work has been done for the study of anisotropic vein formation. For example, the growth of polycrystalline quartz as vein-filling material on rock surfaces in a vein have been modeled using a multiphase-field approach by Wendler et al. (2016) and further by Spruzeniece et al. (2021). In these studies, specially constructed anisotropic functions for surface energy and kinetics were applied to mimic the observed forms of faceted crystals. The crystallization of a dendrite inside the melt droplet in a forsterite-chondrule system was simulated by Miura et al. (2010) by means of the simple phase field model for a pure material. Recently, Miura (2018) used the simple phase field model for a binary system of forsterite and silica where the chemical free energies were approximated by parabolic functions of composition. The growth velocity of the dendrite was investigated in the case of diffusion-controlled and interface-controlled growths.

In the present work, we develop the tool for some simple mineralogical systems which contain many crystals of different orientation, but of the same phase, in a melt. The development includes aspects covered in the earlier studies, but goes beyond to set up a framework for applications in more complex multicomponent, multiphase natural systems containing anisotropic solids. We begin by describing the theoretical background of the model. This part includes some newer developments that are more relevant for mineralogical systems, such as a general exploration of the role of anisotropy of surface/interfacial energies in non-cubic systems. This is followed by some examples of numerical calculations of growth/dissolution of faceted crystals in selected, textbook-type model systems (plagioclase—melt and olivine—melt). We conclude by discussing some implications of our results that emerge, inspite of the simplicity of the modeled systems, for real geological systems. These include aspects of behavior of models of Crystal size distribution (CSD) analysis and diffusion chronometry that have not yet been considered.

2. Phase-Field Method

A complete phase-field method for the modeling of binary and multicomponent systems includes a bulk chemical thermodynamic module (calculation of phase equilibria and deviations from equilibrium), a diffusion module (calculation of transport timescales), and an interface module that accounts explicitly for interfacial energies, that is, capillarity. The last module permits the modeling of mobile interfaces between different phases or crystals of different orientations, and thereby, the evolution of microstructures and textures. This aspect is responsible for the novelty of the tool. In the following, a brief introduction is provided to how interfaces are handled, and references to works where more details may be found are provided, followed by a description of the method used in this study.

The method is based on two basic concepts: "phase field" and "diffuse interface." The phase field is a field in space and time (usually denoted by $\phi(\mathbf{x}, t)$) that indicates the presence of a thermodynamic phase or a crystal grain at each point within the (heterogeneous) volume of interest. For example, in a binary system the phase field is defined as $\phi = 1$ in a solid phase and $\phi = 0$ in a liquid phase (see Figure 1). Knowing ϕ one can determine

the properties of interest (equilibrium chemical composition, geometry of grain boundaries, etc.). The corresponding chemical composition is determined by additional variables which evolve by diffusion equations. If in a system many crystal grains are present which belong to different thermodynamic phases, one can use the notation "phase field" for the thermodynamic phases and "order parameter" for different grains as it was done in Grose and Asimow (2022). In this paper, we use the notation "phase field" as an "indicator variable" which indicates at each point in space and time whether it is occupied by an individual grain $\phi_\alpha = 1$, $\alpha = 1 \ldots N-1$ for $N-1$ possible grains in a multigrain material, and $\phi_L = 1$ for the melt (liquid). Intermediate values indicate interfaces and junctions. The phase fields themselves evolve in time based on the demand for minimization of the free energy of the system. This aspect leads to a few major advantages that make phase-field models particularly useful: (a) the evolution of the system occurs while maintaining internal thermodynamic consistency, (b) grains of different orientations or different phases can be modeled separately by their "own" phase fields ϕ_α, and (c) one deals with scalar quantities rather than vectors with multiple components. "Diffuse interface" is a phenomenological approach where an interface (say, between two crystals, or a crystal and a liquid) is considered to possess a finite width instead of being sharp. In terms of energetics, the consequences are that (a) the interface is a region of finite extent, (b) interfaces between grains or phases move automatically and need not be tracked by hand (c) the interface can possess its "own" properties (e.g., diffusivity), that are distinct from those of the phases bounding an interface, and (d) the phase fields vary smoothly across the boundary and may be represented by continuous, differentiable functions, rather than show a discontinuity at the interface (where the property "jumps" from the value in one phase to that in the adjacent phase). The fourth aspect provides the fundamentally important characteristic that the gradient of a phase field (which is defined as a differentiable function) is related to the curvature and therefore can be related to the velocity of an interface quantitatively in a thermodynamically consistent manner.

A key aspect of the "diffuse interface" models is that they are based on a free energy functional which depends not only on the properties at a given point in the system but also on the local gradient of the phase field around that point

$$\mathcal{F} = \int_V \left[\frac{\epsilon^2}{2} |\nabla \phi|^2 + f_p(\phi) + f_c(\phi, c) \right] dV. \tag{1}$$

$\mathcal{F}$ is the total Gibbs or Helmholtz Free Energy Functional of the system within the volume V. The inhomogeneity $|\nabla \phi|^2$ is also called the "gradient energy," which is also related to the interface energy between grains of different orientations or between different phases, ϵ is the gradient energy coefficient. f_p is the so-called potential operator with two local minima in coexisting phases and an energy barrier between them, which again is related to the interface energy. Examples are "double-well" or "double-obstacle" potentials (Steinbach, 2009). f_c is the bulk free energy density treated here as a function of ϕ and the composition c. It will, in general, also be a function of stress and strain, atomic order on sublattices, magnetism or other fields. It is a task by itself to determine the bulk free energy of a real system as a function of pressure and temperature (taken here as constants prescribed on the system). It will depend on a local minimum condition between the phases, or specify the deviation from local equilibrium which will drive a phase transformation toward the stable phase. In this presentation we will only treat very simple cases, since the focus here lies on the contributions of interfaces and capillarity effects which are offered by the phase-field approach (Steinbach et al., 2007). The driving forces then are specified as deviations of composition and temperature from the equilibrium boundaries on a phase diagram.

Direct coupling to a thermodynamic software, such as CALPHAD (Calculation of PHase Diagramms) (Lukas et al., 2007) has been done routinely and similar approaches may be used to link phase field modeling to commonly used mineralogical thermodynamic databases such as those of Berman (1988) or Holland and Powell (1998) and their later modifications. The tool may also be used in conjunction with free energy minimizing software packages in mineralogical systems such as MELTS (Ghiorso & Sack, 1995), PerpleX (Connolly & Petrini, 2002), or Comagmat (Ariskin et al., 1993). The bottomline is that the use of the phase field model is not restricted to any particular thermodynamic phase diagram, database or program; it is a tool that allows constraints from capillarity and anisotropy of interfaces to be combined with diffusion to quantitatively model the morphological evolution of systems.

The phase field, ϕ, and the two first terms in the free energy functional (1) were originally introduced by Ginzburg and Landau (1950) as an "order parameter" to describe the phase transition of a superconducting material. Then

it was introduced by Cahn and Hilliard (1958) to describe the phase transformation in particular for spinodal decomposition. Later Kobayashi (1993) introduced a first phase-field model for dendritic solidification in an undercooled metallic melt with morphologically unstable growth. The gradient of the phase field in the energy functional makes the formulation non-local and allows changes in the neighborhood of a specific point in space to influence the time evolution of the system. In this regard, the time evolution of the order parameter is governed by the demand for free energy minimization, which is why phase-field models are also called "time-dependent Ginzburg-Landau models":

$$\dot{\phi} = -M_{\phi}\frac{\delta \mathcal{F}(\phi)}{\delta \phi}. \tag{2}$$

Here M_{ϕ} is the interface mobility with units of inverse time multiplied by inverse energy density.

In the same way, we can write down the evolution equation for concentration, which is a conserved order parameter. This equation is also referred to as the Cahn-Hilliard equation (Cahn & Hilliard, 1958),

$$\dot{c} = \nabla M_c \nabla \frac{\delta \mathcal{F}(c)}{\delta c}, \tag{3}$$

where M_c is an atomic mobility.

In more technical terms, conserved quantities (e.g., mass or concentration) are treated using Equation 3 and non-conserved quantities (e.g., phase fields, geometrical properties—Euler angles to characterize interfaces) are treated using Equation 2. The calculation of the temporal evolution of a system requires the use of derivatives of the free energy in the above form, leading to the use of functionals (roughly, a function of a function) and variational derivatives which are defined as

$$\frac{\delta \mathcal{F}}{\delta \phi} = \frac{\partial f}{\partial \phi} - \nabla \cdot \frac{\partial f}{\partial \nabla \phi}, \tag{4}$$

where f is the energy density which is under the sign of the volume integral in Equation 1.

In the following we will generalize the two-phase model introduced before to a multiphase field model, as described in details in the work of Steinbach and Pezzolla (1999), Steinbach (2009). The model can treat an arbitrary number of crystals by using a set of phase fields $\phi_{\alpha}(\mathbf{x}, t)$, limited only by available computer resources. As before, phase fields are defined as $\phi_{\alpha} = 1$ in the bulk α phase/grain and $\phi_{\alpha} = 0$ in other phases/grains. The different grains can belong also to structurally different thermodynamic phases.

The time evolution of phase fields in the multi-phase formalism is constructed following Equation 2 as a sum over all dual interactions between the phases

$$\dot{\phi}_{\alpha} = -\sum_{\beta=1}^{\tilde{N}} \frac{M_{\alpha\beta}}{\tilde{N}} \left(\frac{\delta \mathcal{F}}{\delta \phi_{\alpha}} - \frac{\delta \mathcal{F}}{\delta \phi_{\beta}} \right), \tag{5}$$

where $M_{\alpha\beta}$ is the interface mobility, defined separately for each pair of phases, $\tilde{N}$ is number of phases in a contact point on the interface. The generalization of the free energy functional $\mathcal{F}$ for multiple phases will be presented in the next Section 3, Equation 6.

3. Multi-Phase-Field Model Adopted for the Simulations of the Olivine and Plagioclase Crystal Growth

3.1. Governing Equations

In the present study, the multi-phase field model of Steinbach (2009) has been applied using the open source library *OpenPhase* (OpenPhase, 2023). Here we consider a monomineralic system with $N - 1$ crystals of the same solid phase but different orientations growing in a liquid phase. The crystals are defined by phase fields ϕ_{α} and the liquid is defined by the phase field ϕ_L. The sum of all phase fields in a point in space and time is equal to 1. The crystals can come in contact with each other and form solid-solid interfaces of different misorientations. Individual orientations of crystals are defined in 3D by three Euler angles.

The free energy of a multi-phase system with N phase fields is formulated based on the functional (1)

$$\mathcal{F} = \int_V \left(\sum_{\alpha \neq \beta}^{N} \frac{4\sigma_{\alpha\beta}}{\eta} \left\{ -\frac{\eta^2}{\pi^2} \nabla\phi_\alpha \cdot \nabla\phi_\beta + \phi_\alpha \phi_\beta \right\} + \frac{X(T)}{2} (c - c^{eq}(T))^2 \right) dV, \tag{6}$$

where the first two terms within the brackets set the interface energy $\sigma_{\alpha\beta}$ between the phase fields ϕ_α and ϕ_β, the second term within the brackets is the double obstacle potential. The last term is the chemical free energy density of the bulk material, f_c, which depends on concentrations and temperature T (as well as pressure, P, in principle, but variations of P are not considered in this study). It is treated here in the parabolic approximation of a total free energy density, centered around the equilibrium composition $c^{eq}(T)$ of the system at a given temperature. This is in general a good approximation for diffusion controlled transformations, where the interface is assumed to be in local equilibrium.

The chemical part of the free energy density is the total Gibbs energy of the phases and is defined as a parabolic function of the chemical composition (Kundin et al., 2015). Here, c is the local mixture concentration, c^{eq} is the local equilibrium mixture concentration, defined as a weighted sum on the interface between solid and liquid phases.

$$c = c_S \phi_S + c_L (1 - \phi_S), \tag{7}$$

$$c^{eq} = c_S^{eq} \phi_S + c_L^{eq} (1 - \phi_S), \tag{8}$$

where c_L and c_S are the local concentrations in solid and liquid phases, and c_L^{eq} and c_S are equilibrium concentrations, $\phi_S = \sum_{\alpha \neq L}^{N-1} \phi_\alpha$ is the local sum of all solid phases, $\phi_L = (1 - \phi_S)$ is phase filed responsible for the liquid phase. The sum is taken over all $N - 1$ solid grains, which are the crystals of the same thermodynamic phase.

X in Equation 6 is the mixture thermodynamic factor which is also defined as a weighted sum on the interface between solid and liquid phases

$$X = \left(\frac{1}{X_S} \phi_S + \frac{1}{X_L} (1 - \phi_S) \right)^{-1} = \frac{X_L}{k\phi_S + (1 - \phi_S)} \tag{9}$$

with X_L, X_S being the thermodynamic factors of liquid and solid phases, $k = X_L/X_S$ is the partition coefficient. It can be seen that X becomes X_L in the liquid and X_S in the solid phase.

In the olivine system considered in this study, the temperature is assumed to be homogeneous and constant during simulation. In the plagioclase system, the cooling rate is constant and cooling is considered as series of isothermal steps (see contrasting examples of olivine vs. plagioclase below). The binary phase diagrams are linearized, that is, the slopes of the liquidus and solidus are approximated as linear within the range of interest with a partition coefficient, k, that describes the distribution of components between a solid and a coexisting liquid, that is, $k = dc_S/dc_L = m_L/m_S = X_L/X_S$, where $m_{L/S} = \partial T/\partial c_{L/S}$ are the liquidus and solidus slopes. Note that irrespective of the complexity of a phase diagram, a small segment of the solidus and liquidus lines may always be expressed in a linear form. With these approximations, the equilibrium concentration of liquid and solid phases c_L^{eq} and c_S^{eq} at a temperature T are calculated as

$$c_{L/S}^{eq} = c_{L/S}^{eq}(T_0) + \frac{(T - T_0)}{m_{L/S}}, \tag{10}$$

where T_0 is the liquidus temperature for a given initial composition of the system C_0 (see Figure 2). The linear dependency can be also changed to non-linear functions corresponding to the specifics of any phase diagram with $m_{L/S}(T)$.

After substitution of the functional (6) in Equation 5, we obtain the resulting kinetic equation for a phase field

$$\dot{\phi}_\alpha = \sum_{\beta=1}^{\tilde{N}} \mu_{\alpha\beta} \left(\frac{1}{\tilde{N}} \sum_{\gamma=1}^{\tilde{N}} \left[\sigma_{\beta\gamma}^* - \sigma_{\alpha\gamma}^* \right] \left[\nabla^2 \phi_\gamma + \frac{\pi^2}{\eta^2} \phi_\gamma \right] + \frac{\pi}{\eta} \Delta g_{\alpha\beta} \sqrt{\phi_\alpha \phi_\beta} \right). \tag{11}$$

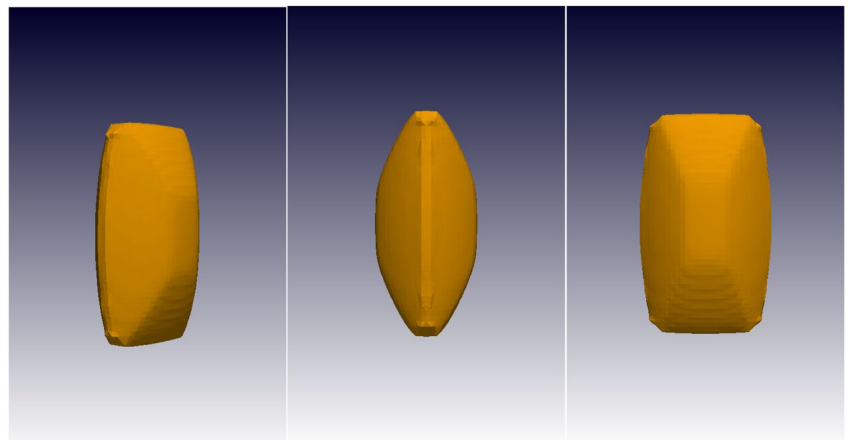

Figure 2. 3-D views of olivine crystals simulated with the (001), (010), (101), (110), and (021) faces.

The mobility $\mu_{\alpha\beta}$ is the rescaled interface mobility in Equation 5 as $\mu_{\alpha\beta} = \frac{8\eta}{\pi^2} M_{\alpha\beta}$. In this paper, we have used constant mobility for all interfaces, that is, $\mu_{\alpha\beta} = \mu_0$. Of course, different mobilities of different interfaces can have a strong influence on the shapes of crystals and the evolution of the microstructure—we leave the exploration of this aspect for future studies.

The last term in Equation 11 is obtained as the derivative over the phase fields of the chemical part of the free energy. The function $\sqrt{\phi_\alpha \phi_\beta}$ is added to guarantee a self similar moving front solution of the dual interface, that is, that it's profile is not deformed during motion (see Appendix of Steinbach (2009)). The driving force, $\Delta g_{\alpha\beta}$, is not zero only for two thermodynamic phases (solid and liquid) and is defined as

$$\Delta g_{SL} = \frac{X_L\left(c_S^{eq} - c_L^{eq}\right)(c - c^{eq})}{k\phi_S + (1 - \phi_S)} = \frac{\Delta S_m m_L (c - c^{eq})}{k\phi_S + (1 - \phi_S)}, \tag{12}$$

where $\Delta S_m = X_L\left(c_S^{eq} - c_L^{eq}\right)/m_L$ is the entropy of transformation. Equation 12 shows two variants to calculate the driving force, first in terms of the thermodynamic factors (see Kundin et al. (2015), for details) and second in terms of the difference in the entropy (see Eiken et al. (2006)). Both variants are appropriate for our study. The multi-phase method can be consistently extended to provide various driving forces, address different extents of anisotropic surface energy, and to consider various grain boundary effects.

$\sigma^*_{\beta\gamma}$ and $\sigma^*_{\alpha\gamma}$ are the stiffness's of the interfaces. Due to anisotropy, the surface energy in the functional (6) is a function of an inclination angle θ, which is the angle between a crystal direction in a crystal lattice and the normal to the interface $\mathbf{n} = \nabla\phi/|\nabla\phi|$. Hence, $\sigma(\theta)$ is a function of gradients, $\nabla\phi$, and by means of Equation 4, it transforms to the 'stiffness' $\sigma^*(\theta) = \sigma + \sigma''$, where σ'' is the second derivative of σ with respect to θ. Note that the stiffness as well as the surface energy is a characteristic of each facet of a crystal. In this paper, we use a special developed anisotropic model for faceted crystals described below in Section 3.3.

By substitution of the energy functional Equation 6 in Cahn-Hilliard Equation 3, one obtains the diffusion equation for the concentration field

$$\frac{\partial c}{\partial t} = \boldsymbol{\nabla} \cdot \left[D\boldsymbol{\nabla} \frac{(c - c^{eq})}{k\phi_S + (1 - \phi_S)} + \mathbf{j}_{\text{at}} \right]. \tag{13}$$

Here $\mathbf{j}_{\text{at}}$ is the anti-trapping current, which is used for the case where the rate of diffusion in the solid is very slow, $D = M_c X \cong (D_S\phi_S + D_L(1 - \phi_S))(k\phi_S + (1 - \phi_S))$ is the mixture diffusion coefficient with D_L and D_S being the diffusion coefficients in the liquid and solid phases, respectively, and M_c is the mixture atomic mobility.

Depending on the application one may start from different thermodynamic functionals such as the Helmholtz free energy, or the Gibbs free energy. Here we treat only problems of phase transformations with fixed temperature and pressure and therefore we use the Gibbs free energy. The chemical part of the free energy density Δg is, in general, defined by the total Gibbs energy of a material point composed of different phases and depends on the

composition (in simple binary systems it is simply the concentration c). It has been typically taken from thermodynamic databases such as CALPHAD (Lukas et al., 2007) for many metallic systems and ceramics and may be connected to databases such as MELTS (Ghiorso & Sack, 1995) for mineral-melt systems.

3.2. Estimation of Interface Mobility

The phase-field models define the velocity of the moving interface by the so-called Gibbs-Thomson equation, which relates the velocity of the interface to the kinetic undercooling (Karma, 2001; Steinbach, 2009) by

$$v_n = \mu(\Delta g - \sigma\kappa), \tag{14}$$

where v_n is the velocity in the direction normal to the interface at a given point, μ is the mobility, σ is the interfacial energy for isotropic systems, Δg is the constant part of the thermodynamic driving force and κ is the mean curvature of the interface. For the anisotropic case, σ should be replaced by the stiffness, σ^*.

The expression for the interface mobility, μ, of a solid-liquid interface for a diffusion-controlled process (in this case, the physical interface mobility is expected to be high) was given by Karma and Rappel (1998), Steinbach (2009), Kundin and Steinbach (2019). For interface-controlled processes, the physical interface mobility is expected to be slow in comparison to the diffusion time scale and μ may be estimated by making use of the Gibbs-Thomson Equation 14.

For the systems investigated in this paper, the crystallization process is interface -controlled, that is, the mobility is slower than for diffusion-controlled growth. To estimate the mobility, we have used the experimental interface velocity at a given undercooling.

3.3. Modeling of the Anisotropic Surface Energy for Faceted Crystals

Grain boundary energies of only a few minerals are known, but it is now becoming possible to calculate grain boundary energies for different crystals using ab-initio simulations, and some examples in the material science literature include (Kim et al., 2011; Lee & Choi, 2004). For faceted crystals, the growth velocity is inversely proportional to the surface energy for a particular facet. The surface energy anisotropy (the dependency of growth rate on the crystal plane) can be estimated using different experimental methods, for example, using experimental crystal growth velocity in different crystal directions. The relative values of the surface energy for different facets can also be estimated using the shape of the crystal using the fact that a distance from the center to a crystal facet is proportional to the surface energy. The absolute value of surface energy can be calculated by atomistic methods (e.g., ab-initio calculations). The surface energy of olivine was calculated, for example, by de Leeuw et al. (2000), Bruno et al. (2014). There are also experimental methods for the definition of grain boundary anisotropy based on the relative abundance of different grain boundary planes in an aggregate (e.g., see Saylor et al. (2000) for an example in MgO, and Marquardt et al. (2015) for olivine). A single experimental study is available on the measurement of interfacial energy between olivine and a basaltic melt (Cooper & Kohlstedt, 1982).

The anisotropic surface energy is responsible for equilibrium shapes of the individual faceted crystals growing in melts and is given by the Wulff construction, which minimizes the total surface energy of the system. The anisotropic model used in this work was suggested by McFadden et al. (1993) and successfully implemented by Salama et al. (2020) for 3-D grain growth. The solid-liquid interface energy of a crystal α is defined as a function of the inclination angle θ_α which is defined in its turn in each point of the moving interface as an angle between the interface normal $\mathbf{n}_\alpha$ and the nearest facet normal $\mathbf{k}^\alpha_{ijk}$. The facet normals are defined at the beginning of the simulation for each particular crystal α depending on its orientation and are represented by Miller indices $\{ijk\}$. The surface energy is then calculated by the anisotropic function of the inclination angle

$$\sigma_\alpha(\theta_\alpha, (ijk)) = \sigma_{ijk}\sqrt{\sin^2(\theta_\alpha) + \kappa^2\cos^2(\theta_\alpha)}, \tag{15}$$

where σ_{ijk} is the maximum surface energy of a facet (ijk), κ is the anisotropy parameter which is smaller for larger anisotropy. This function produces the flat faces of crystals which grow by propagation of planar interfaces in a manner that is different from the mechanism for dendritic growth models.

The different crystal facets have different areas at equilibrium, which should be smaller for facets with larger surface energies. That is because of the minimization of energy during crystal growth. Furthermore, the growth

rate should be faster for a facet with a larger surface energy and smaller surfaces area. In order to capture these relationships, we define the maximum surface energy of a facet (*ijk*) as a function of the surface area ratio, i. e.,

$$\sigma_{ijk} = \sigma_{001}\frac{A_{001}}{A_{ijk}}, \tag{16}$$

where A_{ijk} and A_{001} are the areas of the facets (*ijk*) and (001), respectively, and σ_{001} is the maximum surface energy of the (001) facet which is used as reference energy. In the phase-field model, the growth rate is inversely proportional to stiffness, hence we can assume that the stiffness is directly proportional to the area of a facet. Based on this assumption, we calculate the stiffness σ^* related to the inclination angle as

$$\begin{aligned}\sigma^*_\alpha(\theta_\alpha, \{ijk\}) &= \frac{A^2_{ijk}}{A^2_{001}}(\sigma_\alpha(\theta_\alpha) + \sigma''_\alpha(\theta_\alpha)) \\ &= \sigma_{001}\frac{A_{ijk}}{A_{001}}\kappa^2\left(\sin^2(\theta_\alpha) + \kappa^2\cos^2(\theta_\alpha)\right)^{-\frac{3}{2}}.\end{aligned} \tag{17}$$

Note that the assumption for the stiffness suggested here is a simplification with a clear physical meaning.

The model above is valid for single crystals in melts. To calculate the interface energy between two crystals that are in contact, we define a solid-solid interface energy $\sigma_{\alpha\beta}$ as a mean value of two solid-liquid interfaces

$$\sigma_{\alpha\beta} = \frac{r_{sl}}{2}(\sigma_\alpha + \sigma_\beta), \tag{18}$$

where r_{sl} is the ratio between solid-solid and solid-liquid interface energies. Usually, the energy of solid-solid interface is larger, resulting in $r_{sl} > 1$. Then, in a similar way, the stiffness of the boundary between solids is defined as

$$\sigma^*_{\alpha\beta} = \frac{r_{sl}}{2}\left(\sigma^*_\alpha + \sigma^*_\beta\right). \tag{19}$$

In the case of small misorientation angles, interface energy decreases very fast as the misorientation angle decreases. To mimic this behavior, we define the ratio r_{sl} for misorientations $\theta_\alpha - \theta_\beta < 5°$ equal to $r^{\mathrm{m}}_{sl} = 1$.

3.4. Evaluation of Crystal Size Distribution (CSD)

The crystal size distribution (CSD) is defined by the number of crystals within a given size interval per unit area divided by the length interval (bin width) (Higgins, 2000, 2006), that is,

$$n_V(L) = \frac{N(L_{XY})}{|L_X - L_Y|V}, \tag{20}$$

where $N(L_{XY})$ is the total number of crystals in the simulation domain in the size interval L_X to L_Y, $|L_X - L_Y|$ is the bin width, and V is the domain volume.

The parameter $n_V(L)$ is called the population density and has units of $1/\mathrm{L}^4$. The corresponding CSDs are usually plotted as ln(population density) versus crystal size (Cashman, 2020; Marsh, 1988).

4. Numerical Results

We illustrate the capabilities of phase-field modeling using two common petrological systems—the olivine—melt system and the plagioclase—melt system. We underscore that interfacial energies playing a central role in phase-field calculations are not well known in most mineralogical systems. For illustration here, we have guessed values for the relevant energies that may yield textural appearances that correspond to those frequently observed in natural systems. The values for olivine were chosen to be in the range expected from the study of Cooper and Kohlstedt (1982). The point of this exercise is two-fold. First, to encourage the experimental measurement of the relevant parameters given the availability of this tool. Second, in natural systems where all other parameters may be independently constrained, model fits may be used to infer/constrain the values of the relevant interfacial energy parameters. The second exercise may provide a means of evaluating the range of variability of interfacial energy parameters in natural systems, and help to identify critical systems for detailed experimental studies.

Table 1
Model Parameters for the Systems Olivine—Melt and Plagioclase—Melt

Parameter	Symbol	Olivine	Plagioclase	Units
Grid spacing	Δx	1×10^{-5}	1×10^{-5}	m
Time steps	Δt	5	5×10^{-2}	s
Interface width	η	$5\Delta x$	$5\Delta x$	m
Surface energy	σ_{001}	2.45	1.00	J m^{-2}
Surface energy	σ_{100}	1.22	0.12	J m^{-2}
Ratio between energies	r_{sl}	1.5 and 4	1.5	–
Anisotropy strength	κ	0.2	0.173	–
Interface mobility	μ_0	1×10^{-13}	2.5×10^{-12}	m^4 (J s)$^{-1}$
Diffusion coefficient in liquid	D_L	3×10^{-12}	3×10^{-10}	m^2 s^{-1}
Diffusion coefficient in solid	D_S	3×10^{-16}	3×10^{-16}	m^2 s^{-1}
Initial concentration in melt at T_0	$C_L^{eq}(T_0)$	73 (Fo)	74 (An)	wt. %
Initial concentration in crystals at T_0	$C_S^{in}(T_0)$	90 (Fo)	90 (An)	wt. %
Equilibrium concentration in melt at T	$C_L^{eq}(T)$	62 (Fo)	72 (An)	wt. %
Equilibrium concentration in crystals at T	$C_S^{eq}(T)$	85 (Fo)	89 (An)	wt. %
Liquidus slope	m_L	−4.6	−2.0	K/wt%
Solidus slope	m_L	−12.8	−5.0	K/wt%
Partition coefficient	k	0.36	0.40	–
Molar volume	V_m	43	101	cm^3 mol^{-1}
Entropy of transformation	ΔS_m	1.6	1.0	J cm^{-3} K^{-1}
Liquidus temperature	T_0	1,830	1,553	°C
Initial undercooling	$T_0 - T$	50	5	K
Cooling rate	$\dot{T}$	0	0.02	K/s

4.1. Olivine—Melt System

The model parameters are listed in Table 1. The calculations were carried out for a melt of composition 73 wt.% Forsterite with a constant undercooling of 50 K (i.e., at a constant temperature of 1725°C). The diffusion coefficient is chosen as in silicate melts circa 10^{-12} m^2/s (Dingwell, 2006). The mean growth rate of olivine crystals, υ_n is assumed as 10^{-5} m/s (Zieg & Lofgren, 2002). The interface mobility is defined at the undercooling 10 K as $\mu = \upsilon_n/|\Delta S_m(T_0 - T)| \sim 10^{-13}$ m^4(Js)$^{-1}$. This value is close to the diffusion controlled growth. No flux boundary conditions in all directions are chosen for all fields. The liquidus slope and the partition coefficient is calculated from the experimental phase diagram in Figure 3 and from Ford et al. (1983). The entropy is calculated from the cryoscopic equation (Philpotts, 1988) as

$$\Delta S_m = \frac{2R}{V_m} \ln\left(\frac{X_{\mathrm{E}}^L}{X_{\mathrm{E}}^S}\right)\left(1 - \frac{T_m^{\mathrm{A}}}{T}\right), \tag{21}$$

where R is the gas constant, V_m, is a molar volume T_m^{E} is the melting temperature of an end-member, X_{E}^L and X_{E}^S are the liquid and solid equilibrium molar fraction of the end-member at a temperature T. The surface energy of olivine crystals is taken from Lilova et al. (2018). A ratio between solid-solid and solid-liquid interface energies is chosen as $r_{sl} = 1.5$.

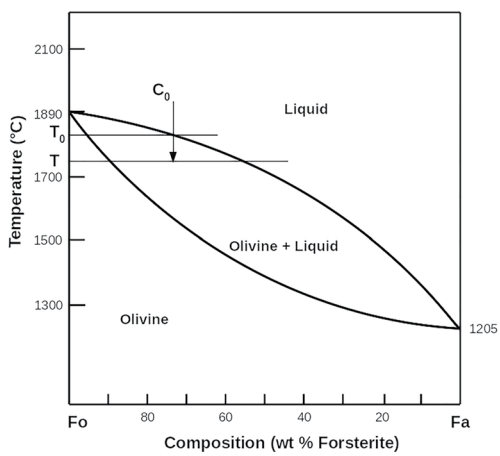

Figure 3. Phase diagram of the Fo-Fa system and the thermodynamic history used in the simulation of olivine crystals.

4.1.1. Single Olivine Crystal Shape

To model the shape of the real olivine crystals from Welsch et al. (2012), we use the following surface area ratios estimated from the experimental pictures:

faces	(001)	(100)	(010)	(101)	(110)	(021)
A_{ijk}/A_{001}	1	0.5	1.67	0.83	2.33	2.26

The simulated shape of a single olivine crystal is shown in Figure 2. It is formed by using a driving force that depends on the change of the crystal volume by $\Delta G \sim (V - V_0)/V_0$, where V_0 is an initial crystal volume. An initially round crystal of radius $20\Delta x$ was placed in a cubic domain of size $66 \times 66 \times 128\Delta x$. After 2,000 time steps (ts), the crystal shape transforms to the equilibrium one following the chosen anisotropic surface energy parameters. In numerical simulations, we will use this algorithm to balance the shape of seeds before running the main simulation loop."

4.1.2. Solidification of a System of Olivine Crystals

In the following, we present the simulation of the monomineralic solidification of olivine crystals in a basaltic melt. An exponential distribution of nuclei (Hersum & Marsh, 2006, 2007) is modeled by the generation of seeds of random sizes distributed by exponential law and randomly distributed in space. The random size of seeds is defined as $R_0 = (7 + 0.5 \cdot 10^{1.3\ \delta})\Delta x$, where δ is a random number from 0 to 1. This method produces an exponential distribution of seeds which then results in a linear crystal size distribution, as used in the theoretical models of crystallization in rocks (Higgins, 2000). To avoid the contact of seeds (pure homogeneous nucleation), the distance between the seeds is limited to $20\Delta x$. The scheme of the phase diagram with the initial composition C_0 and the liquidus temperature for this composition T_0 is shown in Figure 3. We assume that seeds are formed at higher undercooling, and hence they have initial compositions that are different from the equilibrium composition at temperature T. Here we track the crystallization in a closed system with a constant bulk composition of 73 wt.%Fo.

Simulation 1 was carried out in a cubic domain of size $186^3\Delta x$ with 320 seeds. The simulated microstructure is shown in Figure 4 as 3-D views at the different time steps (ts): 5,000 s (1,000 ts), 30,000 s (6,000 ts), and 70,000 s (14,000 ts). The corresponding 2-D slices through the 3-D microstructure with the concentration field are shown in the second row of Figure 4. 2-D slices correspond to different faces of 3-D plots. On 2-D slices, we can see anisotropic crystals of different orientation. The concentration of fayalite in crystals is different in the center and along the edge. This is due to the fact that the initial concentration of seeds was chosen at a temperature below the solidification temperature. Due to the small diffusion coefficient in a solid, diffusion between different areas of concentration is slow.

In Simulation 2, the system size is increased to $276^3\Delta x$ and the number of seeds to 580. We specifically took different densities of seeds as an example to show that it does not affect the quality of the CSD. The simulated microstructure as 3-D views of crystals and 2-D slices of the concentration field is shown in Figure 5 at different time steps. The CSDs for both tests are shown in Figure 6. It can be seen that CSDs change similarly with time in both simulations. Hence the system size and the density of seeds do not influence the texture. The initial number of crystals decreases during crystallization and the CSDs change from the linear to the parabolic form. That means that an initially imposed exponential distribution of crystal sizes is not retained during grain growth. This is because the growth rate depends on the crystal size, so that the small crystals dissolve and the larger crystals grow faster. The time evolution of the solid fraction for Simulations 1 and 2 are compared in Figure 7. The solid fraction goes to its equilibrium value for the given undercooling. In the second test, we started with a smaller solid fraction, however, the slope of the time dependence is similar to the first simulation test, reflecting a similar average growth rate.

4.1.3. Effect of the Solid-Solid Interface Energy

The ratio between solid-solid and solid-liquid interface energies affects the ability of crystals to bind to each other. In order to study this behavior, we carried out the Simulation 3 in the domain size of $186^3\Delta x$ with 480

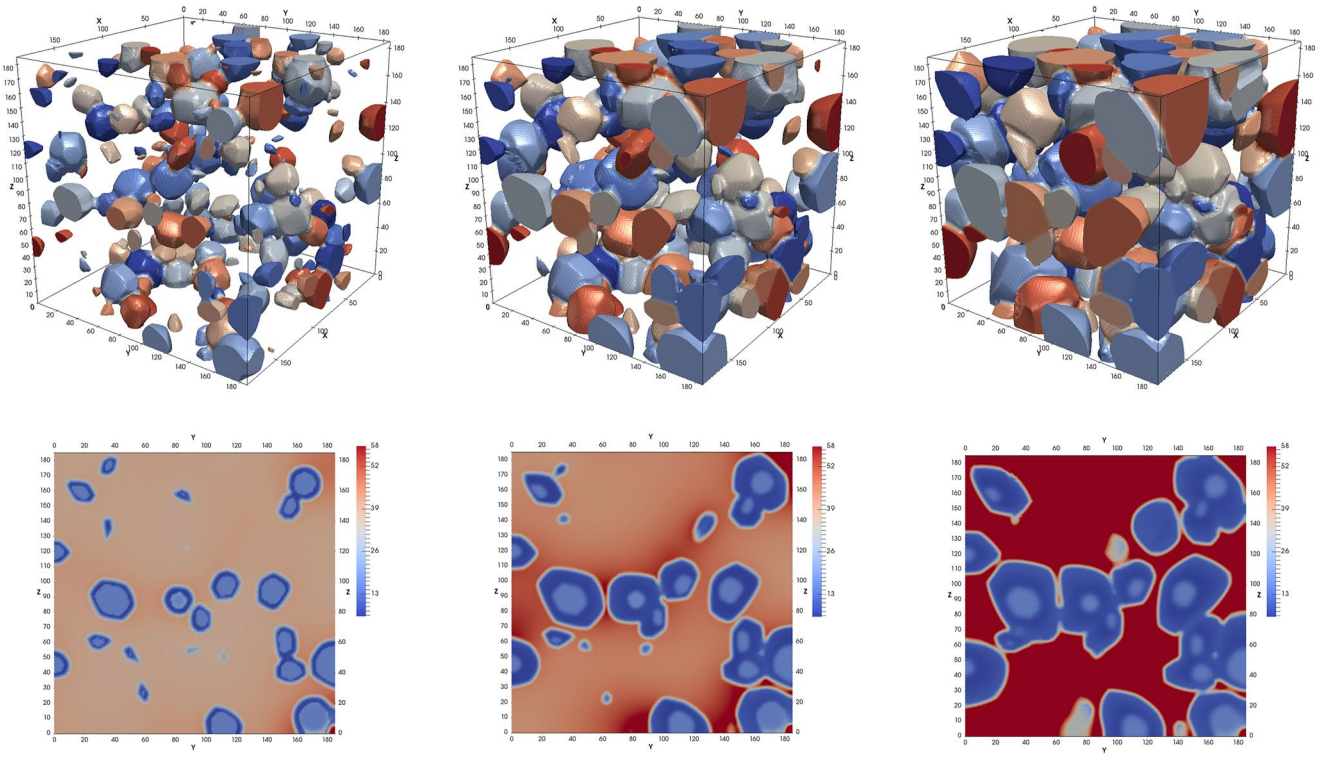

Figure 4. 3-D views of the microstructure of the olivine crystals and 2-D slices with the concentration fields of fayalite in Simulation 1 at 5,000 s, 30,000 s, and 70,000 s. Colors in 3-D represent the phase fields. The system size is 1,860 μm in each direction.

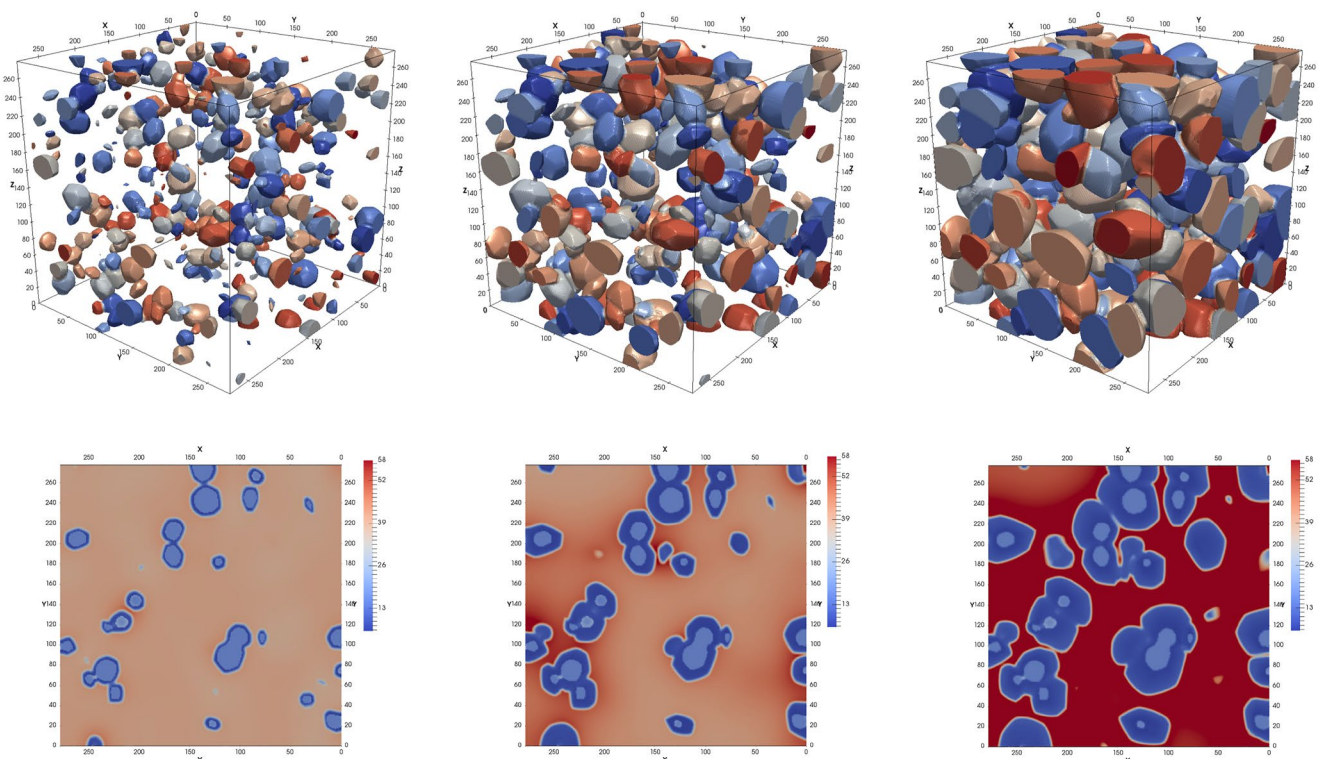

Figure 5. 3-D views of the microstructure of the olivine crystals and 2-D slices with the concentration field of fayalite in Simulation 2 at 5,000 s, 30,000 s, and 70,000 s. Colors in 3-D represent the phase fields. The system size is 2,760 μm in each direction.

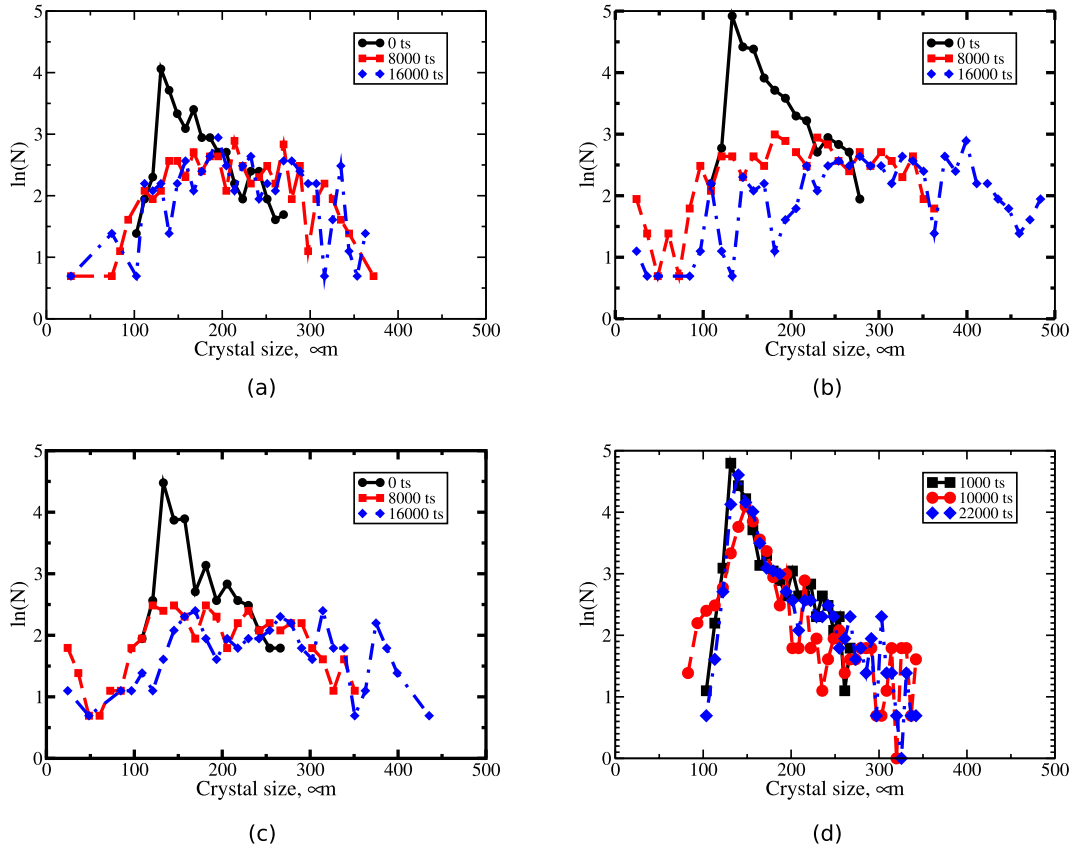

Figure 6. Time evolution of CSDs in Simulation 1 (a), Simulation 2 (b), Simulation 3 (c), Simulation 4 (c).

initial seeds of random size. The ratio is increased to $r_{sl} = 4$. The simulated microstructure (phase fields) is shown in Figure 8 at times 5,000 s (1,000 ts), 30,000 s (6,000 ts), and 75,000 s (15,000 ts) that correspond to the solid fractions 19%, 35%, and 61% respectively. The corresponding 2-D slices with the concentration field are shown in Figure 8 on the bottom. The main difference with the previous simulation runs is that the crystals do not bond to each other, and a thin layer of melt of size from 4 to $5\Delta x$ remains between the crystals. The CSDs and the crystal fraction evolve with time in the same manner as in previous tests (see Figure 6c).

Future work is necessary to compare the simulated microstructures with experimental data and estimate the ratio between the solid-solid and solid-liquid interface energies. Furthermore, one should take into account the minimum interface energy at small misorientations between crystals that results in the formation of groups of intergrown crystals of the same orientation as it was observed in the work of Welsch et al. (2012).

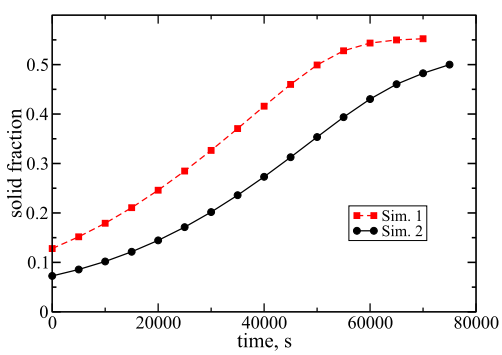

Figure 7. Time evolution of the crystal fraction of olivine in Simulations 1, 2.

4.1.4. Effect of the Interface Mobility

In Simulation 4 we demonstrate how the phase-field model can reproduce the linear CSDs observed in experiment. Here we will refer to the work of Zieg and Lofgren (2002), where olivine growth rates were measured during the solidification experiment versus the crystal length. Using these experimental data, we have included in the model the dependency of the interface mobility on the crystal size as $\mu_{\alpha L} = \mu_0 V_\alpha(t)/L_0^3$, where $V_\alpha(t)$ is the current volume of a crystal and $L_0 = 300$ μm is a reference crystal length. Such dependency can be caused by the strong anisotropy and the epitaxial growth of crystal facets. Future study of this behavior in mineral systems is needed which is completely different from the dendritic growth in metals. The test was carried

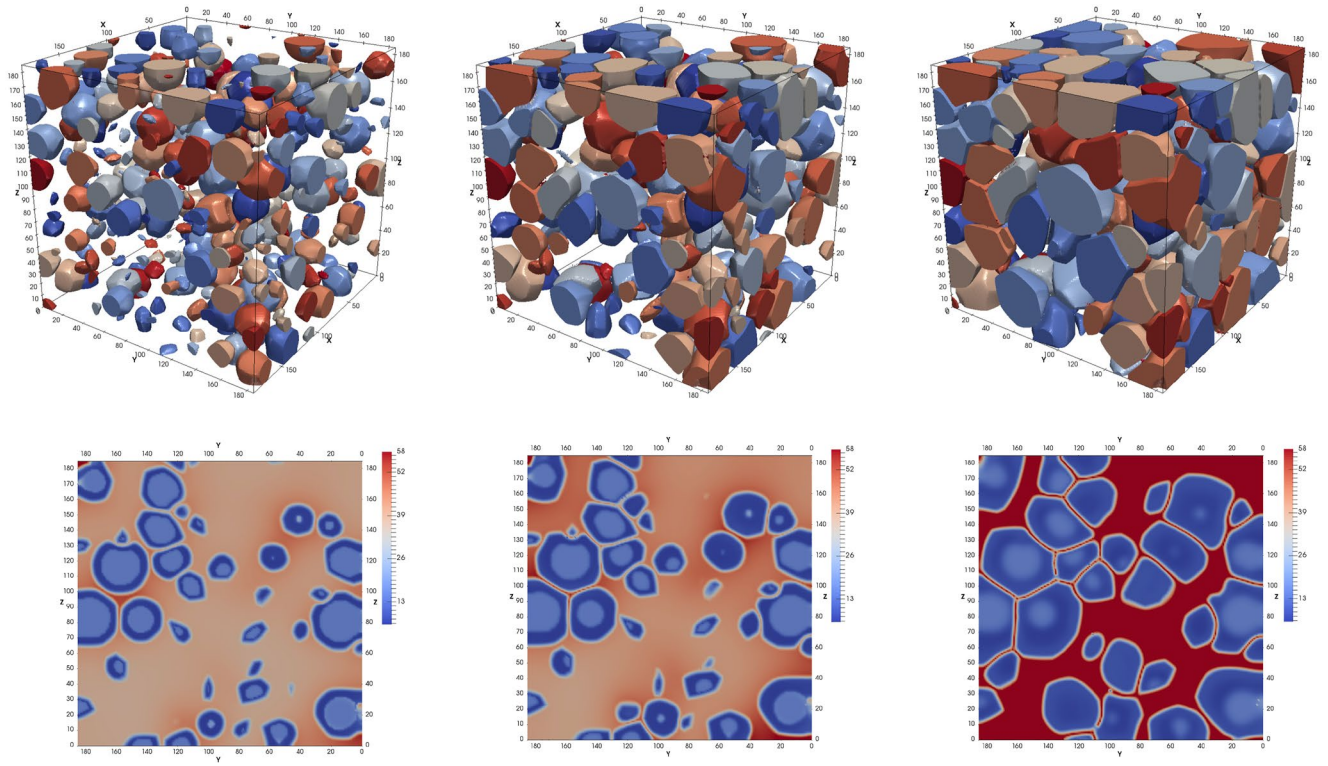

Figure 8. 3-D microstructure of the olivine crystals and 2-D slices with the concentration field at times 5,000 s (1,000 ts), 30,000 s (6,000 ts), and 75,000 s (15,000 ts) in the simulations with the large ratio $r_{sl} = 4$. Colors represent the phase fields. The system size is 1,860 μm in each direction.

out in the same system as in Simulation 2: the size $276^3\Delta x$, 580 seeds. The results are shown in Figure 6d. The CSDs keep the linear form, the right side of the dependency expands with more large crystals. The small crystals do not grow and do not dissolve, they remain in the system due to the slow interface mobility. The simulated CSDs evolve similar to the experiment, as expected.

4.2. Plagioclase—Melt System

The model parameters that were used in the calculations are listed in Table 1. The diffusion is chosen to be faster than in the previous system. The anisotropy of the triclinic symmetry of a plagioclase crystal is modeled by two facets (100) and (001) with different surface energies. In contrast to the previous example, here we track the crystallization in the plagioclase system for a closed system with a constant bulk composition of 74 wt.%An for a constant cooling rate of 0.02 K/s. The numerical simulation was carried out in a rectangular domain of size $200 \times 520\Delta x$ (2,000 × 5,200 μm). The phase diagram of the plagioclase—melt system and the initial composition are illustrated in Figure 9. The slopes of boundaries in the phase diagram are approximated by linear functions. The entropy ΔS_m is estimated by Equation 21 at the middle of the solidification interval. The surface energy is taken from Taniguchi (1988). Figure 10 shows a series of stages (abundance of phases, orientation of crystals and compositions of crystals and melt in each case) in the calculated evolution of the system for different temperatures. We introduce 44 circular seeds, each with a radius of $R_0 = 10\Delta x$, at random positions in the system. The initial concentrations in seeds and the liquid phase are at equilibrium at the undercooling of 5 K. Then we let them grow without thermodynamic driving force to form the anisotropic shape as described in

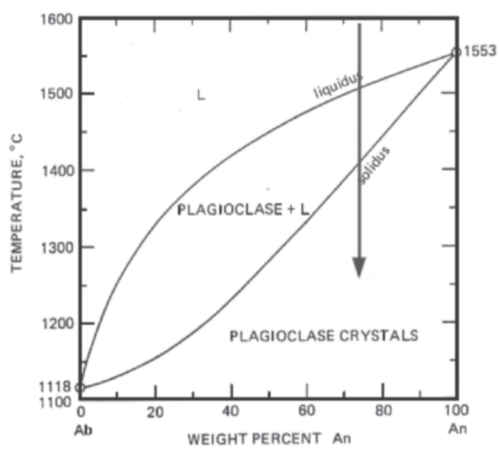

Figure 9. Plagioclase phase diagram. The arrow shows the initial concentration of the system.

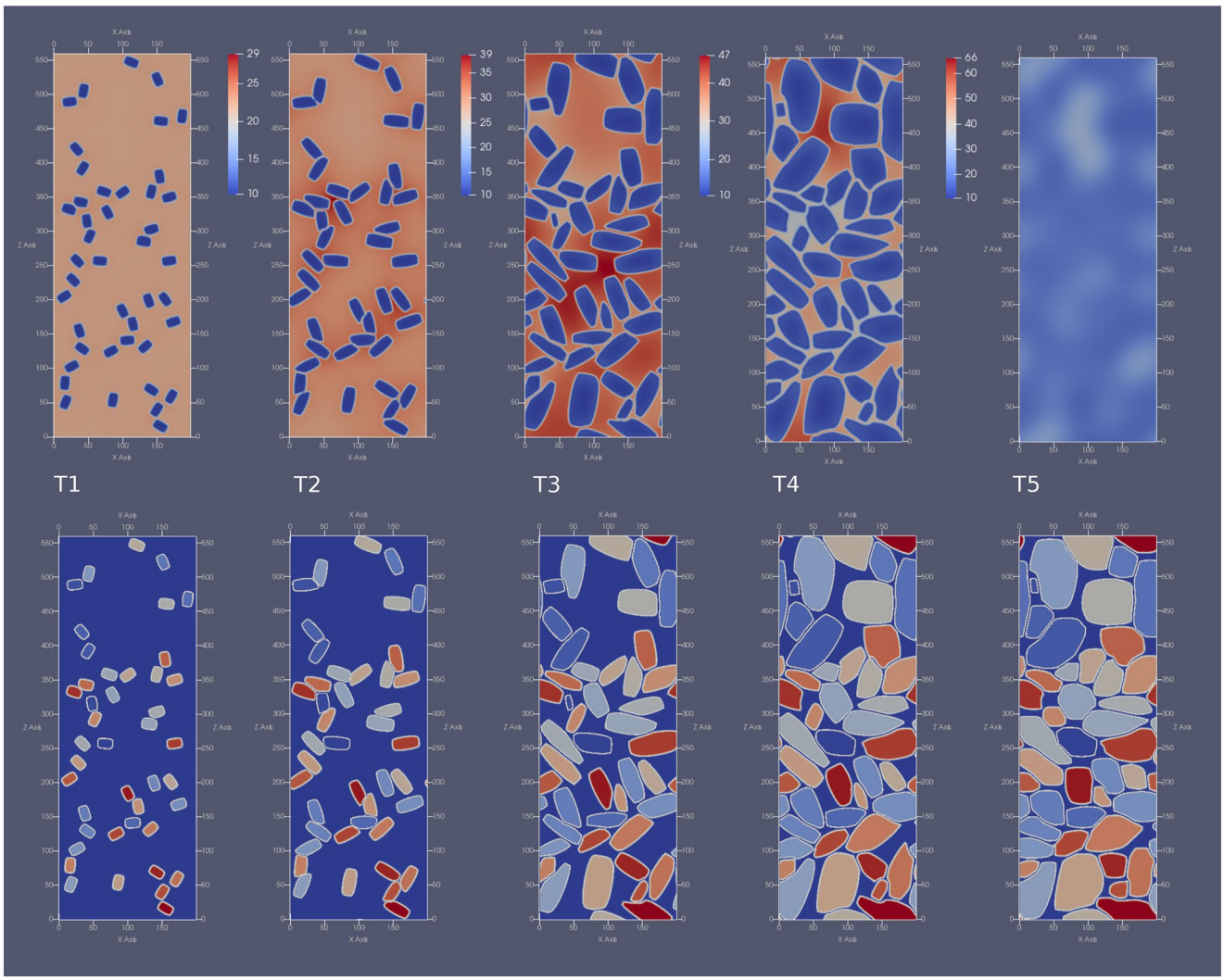

Figure 10. 2-D microstructure of the plagioclase crystals with the concentration field (top row) and the phase field (bottom row) at various undercoolings during the cooling process: 5 K (T1), 23 K (T2), 41 K (T3), 53 K (T4), and 77 K (T5); the cooling rate is 0.02 K/s, the corresponding time is 0 s, 900 s, 1,800 s, 2,400 s, 7,200 s + 4,800 s. The system size is 2,000 μm in x-direction and 5,200 μm in z-direction. Color bars represent the concentration of Albite.

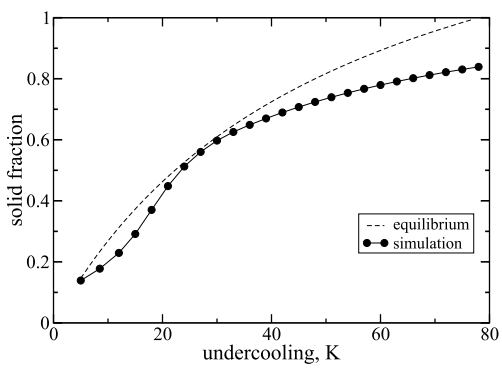

Figure 11. Evolution of the crystal fraction of plagioclase as a function of the undercooling. Equilibrium case and the simulation results with the cooling rate 0.02 K/s.

Section 4.1.1. Then the cooling turns on with the cooling rate 0.02 K/s, and the simulations proceed till the solidus line at the undercooling of 77 K.

The simulation results, the shapes of crystals and their compositions are shown in Figure 10 at different temperatures $T = \{T1,T2,T3,T4,T5\}$, which corresponds to undercoolings $\Delta T = \{5, 23, 41, 53, 77\}$ K and times $t = \{0, 900, 1{,}800, 2{,}400, 7{,}200 + 4{,}800\}$ s. The evolution of solid fraction during the cooling process is plotted in Figure 11 in comparison to the equilibrium calculations (level rule). At the temperature T5, the system is subjected to homogeneous annealing at the constant undercooling for an additional time equal to 4,800 s. The liquid phase is assumed to be solidified. During this annealing process the composition in the system is homogenized. To accelerate the homogenization, the diffusion coefficient is changed to 3×10^{-10}. Figure 12a shows the crystal size distribution in the system as the number of crystals in a size interval (one bin of the histogram equals 80 μm), and Figure 12b shows CSD as the crystal population density by Equation 20.

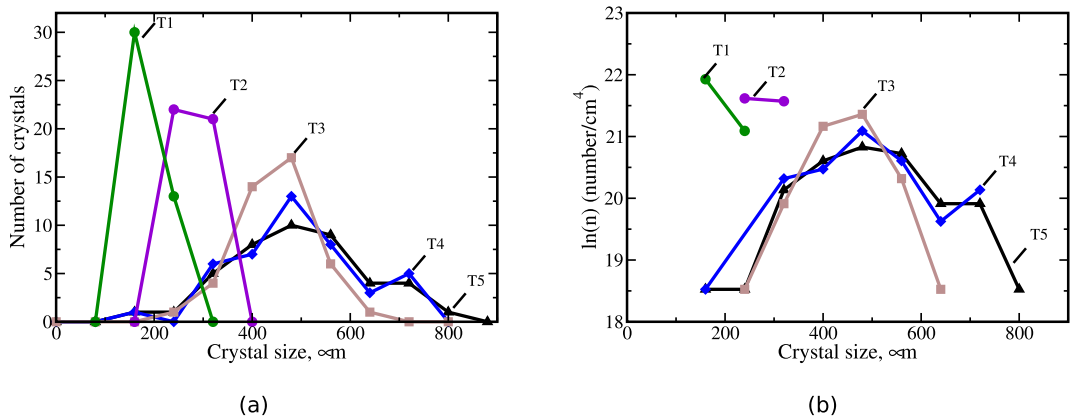

Figure 12. CSD in plagioclase system during the cooling process with linear (a) and logarithmic scale (b) on the *y*-axis.

At T1, where 14% of the system should crystallize at equilibrium, the anisotropic seed crystals (in accordance with the chosen difference in interfacial energies—see Table 1) begin to grow. At T2, 50% of the system crystallizes at equilibrium, and the calculation shows growth of crystals to larger sizes. The simulated solid fraction in this region is far behind that expected at equilibrium. Noticeable is the fact that the composition of the liquid at a particular point in space depends on the thermodynamic (and kinetic, through diffusion) interaction with the neighboring grains. Such interaction influences the growth rate of any given crystal and its shape. With further evolution, at T3 (66% crystallization), the growth continues and the crystal size distribution becomes more dispersed. The competition of growth between crystals produces some very large as well as some very small crystals. At T4 (85% crystallization), one has a compact crystal mush where the local compositional variation is very apparent. This has important implications for the compositions and shapes of subsequent plagioclase that grows from the melt. At T5 (100% crystallization), the solidus is reached and there should be no remaining liquid in equilibrium. However, there is still liquid present in the simulation due to the anisotropy of crystals (i.e., different crystal surfaces have different energies and therefore some may still coexist with liquid at this temperature). In reality, the nucleation process may proceed between T2 and T5. Beyond this point, there are no significant changes in grain size of crystals but the compositions of the zoned crystals continue to evolve by diffusion. The extent of this depends obviously on the cooling rate and is an important parameter for diffusion chronometry.

Overall, the crystal size distribution evolves to larger sizes and becomes more dispersed with progressive crystallization in the system. The change in crystal size distribution is a direct consequence of the competition between crystals for growth as the available volume of liquid reduces with progressive crystallization, as well as the attempt to minimize surface energies in the overall system through processes such as Ostwald ripening. During this evolution, some early formed smaller crystals disappear to enable the growth of larger crystals. Thus, the lifetime of a given crystal in the system is variable, and this aspect has important implications for diffusion chronometry.

The calculated microstructure at low temperatures can be qualitatively compared to the nature of observations and theoretical predictions in Morse et al. (2017), for example, the liquid fraction, the composition profiles.

Features such as the extent to which local melt compositions get trapped in growing crystals, whether they crystallize according to the locally available composition or approach the expected equilibrium composition, and whether the distribution of melts wets grain boundaries or form more isolated pockets depend on the values of the various thermodynamic and kinetic parameters and their relative magnitudes (e.g., cooling rate, interfacial energies, diffusion rates in melts, among others).

5. Discussion

The results above demonstrate that a formal quantitative structure that permits the calculation of textural evolution taking thermodynamic constraints into account for complex, anisotropic mineralogical systems is in place. The parameters that are necessary to perform such calculations have been enumerated, and gaps in knowledge—mainly in our knowledge of various surface energy/interfacial energy parameters—have been identified. We have

also outlined various approaches that may allow these quantities to be determined. This includes the possibility of documenting the distribution of grain boundaries of different orientations in natural rocks to infer the relative magnitude of anisotropy in interfacial energies in a mineral (e.g., see Marquardt et al. (2015) for the method).

5.1. Implications for Crystal Size Distribution (CSD) Analysis

A main advantage of the approach outlined here is that although nucleation behavior remains externally imposed (i.e., arbitrary), the growth rates obey local thermodynamic and geometrical constraints. Our calculations show that the form of crystal size distributions (CSD) depends on a competition between the thermodynamic driving forces and surface energy terms that try to reduce the energetic costs of creating surfaces, particularly surfaces with higher energies (in an anisotropic system). As a result, growth rates depend on sizes of crystals and are inversely related to the curvature of a crystal surface. We note that this aspect remains irrespective of whether the growth overall is by diffusion-controlled or an interface-controlled process. The general outcome is that growth rates are not constant during the evolution of a system, and that can result in a change of slope in a CSD plot. Cashman (2020) discusses various possibilities that may give rise to such breaks in natural systems, the results obtained here provide additional alternatives. Linear CSD patterns may be expected only for limited extents of crystallization. A number of new behaviors emerge as a consequence of non-constant growth rates. For example, some smaller crystals dissolve to facilitate the growth of larger crystals (a process akin to Ostwald ripening) and growth rates react to depletion/enrichment of certain components in the melt in the immediate vicinity of a growing crystal (e.g., see Figure 5). This extent of depletion/enrichment is controlled, in turn, by the diffusivity of the relevant elements in the melt and factors that control its physical dynamics (e.g., viscous flow, buoyancy effects)—thus, these models provide a connection between growth rates and the behavior of the melt in the system in which growth takes place. All of these aspects would influence the textural evolution of a natural system and as a consequence, the CSD that is measured.

5.2. Implications for Melt-Inclusion and Mush Zone Studies

Our results with different values of interfacial energies, keeping other factors the same (e.g., Figure 8) show how melt films may separate two adjacent crystals for the certain values of this parameter. This aspect, and also the local enrichment/depletion effects discussed above, may cause a variety of different compositions to be trapped as melt inclusions in crystals growing in a closed system. In other words, external input of melt of a different composition is not necessarily required to produce melt inclusions with a wide range of compositions (see Wieser et al. (2020) for some related situations).

Phase-field simulations are sensitive to the orientation of individual crystals, since their shape depends critically on the interface energy anisotropy as a function of misorientation and inclination: surfaces and their properties play a central role in these calculations. Therefore, calculations such as those shown in Figure 5 may be used to distinguish between mush zones that have crystallized in situ, versus cumulate piles that may have been produced by sinking crystal in a magma reservoir (e.g., see Wieser et al. (2019)). How the combination of expected compositional zoning and orientation distributions of crystals differ in those two situations would be a particularly powerful petrogenetic tool.

5.3. Implications for Compositional Zoning in Crystals and Diffusion Chronometry

In the simulations in this study we produced the seeds with considerable undercooling, so that the composition of the seeds were far removed from the equilibrium compositions expected at the given temperature. This automatically produces compositionally zoned crystals because subsequently grown sections of the crystals form with the equilibrium compositions. The nature of such zoning is controlled by (a) the degree of undercooling, (b) the rates of diffusion of the relevant elements in the crystals, and (c) the time available for evolution (e.g., cooling rate, annealing time). These controls on the compositional zoning pattern observed in a crystal are critical inputs in diffusion chronometry but have not been explored yet in this context to any large extent. We demonstrate that phase-field modeling provides a path toward better understanding of this phenomenon.

Finally, and perhaps most importantly from the perspective of studies of timescales of magmatic processes, this tool promises to provide a bridge between determination of timescales using CSD analysis and diffusion

chronometry. Both, CSD patterns and compositional zoning patterns are calculated as part of the same internally consistent and to the extent permitted by availability of data, thermodynamically real calculations. We find, for example, that crystals do not grow monotonously since their time of nucleation. Instead, the population evolves through dissolution of some crystals and growth of others, and with different growth rates in different parts of the system. The direct consequence of this is that crystals of different sizes may have different growth zoning patterns and may have experienced diffusion for different lengths of time. The important consequence is that the lifetime of a given phase (say, olivine or plagioclase in the simulations considered in this study) in a system is different from the lifetime of a particularly crystal of the phase. In a magma reservoir residing for, say, 50 years at conditions defined by a given set of intensive thermodynamic variables (P, T, f_{O_2},…etc.) a phase such as olivine may be stable; but textural maturation involving dissolution and growth of crystals may have been completed much later, such that a given crystal of olivine may have been in place for, say, only 10 years. Then, 10 years is the maximum timescale that may be obtained from diffusion chronometry of olivine, using any chemical element. Thus, there is an inherent upper limit to timescales that may be accessible by diffusion chronometry of a given phase. This aspect has not been recognized yet but is crucial for application of diffusion chronometry in different settings. Phase field simulations provide a means of exploring that limit to timescales accessible by diffusion chronometry.

6. Conclusion

In this study we have developed a framework for doing phase field calculations with minerals of complex chemistry and anisotropic crystal forms in isothermal as well as non/isothermal systems. The calculations permit the morphological and textural evolution of mineral - melt (or mineral—mineral) systems to be tracked maintaining internal consistency with thermodynamic phase equilibria relationships and diffusive mass transport between different parts of the system. Illustrations using common phase diagrams in petrology reveal some general behaviors that are relevant for applications in natural systems. For example, crystal growth at constant rates is found to occur over only limited ranges of crystallization if consistency with thermodynamic and diffusive mass transport relationships are maintained. This has important implications for the interpretation of crystal size distribution (CSD) patterns of natural systems. Kinetic controls on the development of compositional zoning in minerals (e.g., due to degrees of undercooling, diffusion rates of elements in minerals or in the surrounding melt) can be modeled on a grain by grain basis. This aspect allows the occurrence of different kinds of zoning patterns in different grains of the same mineral undergoing a given thermal history, or the occurrence of different melt compositions (e.g., as inclusions) in the course of such evolution, to be better understood in a quantitative manner. The overall textural evolution may be useful in distinguishing between crystal formed in-situ in a mush zone from those that formed as a cumulate. All of these aspects have fundamental implications for timescales accessible to diffusion chronometry, and they provide a bridge between the two commonly used tools of CSD analysis and diffusion chronometry in magmatic systems.

Data Availability Statement

The developed software is a part of the open source library *OpenPhase* (OpenPhase, 2023) as examples of the solidification of olivine and plagioclase systems. It can be downloaded from http://www.openphase.de.

Acknowledgments
We would like to thank the Deutsche Forschungsgemeinschaft (DFG, German Research Foundation) for funding this research through the Forschungsgruppe "Diffusion Chronometry of Magmatic Systems" under projects FOR 2881/1 and KU 3122/4-1. The authors thanks Oleg Shchyglo for help in adapting the program. Open access funding enabled and organized by Projekt DEAL.

References

Amenta, R. V. (2001). Three-dimensional computer modeling of fabric evolution in igneous rocks. *Computers & Geosciences*, *27*(4), 477–483. https://doi.org/10.1016/S0098-3004(00)00075-3

Amenta, R. V. (2004). Computer modeling of igneous hypidiomorphic textures using crystal prisms and plates with comparisons of measured crystal size distributions. *AGU Spring Meeting Abstracts*, V43C-03.

Amenta, R. V., Ewing, A., Jensen, A., Roberts, S., Stevens, K., Summa, M., et al. (2007). A modeling approach to understanding the role of microstructure development on crystalsize distributions and on recovering crystal-size distributions from thin slices. *American Mineralogist*, *92*(11–12), 1936–1945. https://doi.org/10.2138/am.2007.2408

Ariskin, A., Frenkel, M., Barmina, G., & Nielsen, R. (1993). COMAGMAT: A Fortran program to model magma differentiation processes. *Computers & Geosciences*, *19*(8), 1155–1170. https://doi.org/10.1016/0098-3004(93)90020-6

Berman,R.G.(1988).Internally-consistentthermodynamicdataformineralsinthesystemNa2O-K2O-CaO-MgO-FeO-Fe2O3-Al2O3-SiO2-TiO2-H2O-CO2. *Journal of Petrology*, *29*(2), 445–522. https://doi.org/10.1093/petrology/29.2.445

Boettinger, W. J., Warren, J. A., Beckermann, C., & Karma, A. (2002). Phase-field simulation of solidification. *Annual Review of Materials Research*, *32*(1), 163–194. https://doi.org/10.1146/annurev.matsci.32.101901.155803

Bruno, M., Massaro, F. R., Prencipe, M., Demichelis, R., De La Pierre, M., & Nestola, F. (2014). Ab initio calculations of the main crystal surfaces of forsterite (Mg2SiO4): A preliminary study to understand the nature of geochemical processes at the olivine interface. *Journal of Physical Chemistry C*, *118*(5), 2498–2506. https://doi.org/10.1021/jp409837d

Cahn, J. W., & Hilliard, J. E. (1958). Free energy of a nonuniform system. I. interfacial free energy. *The Journal of Chemical Physics*, *28*(2), 258–267. https://doi.org/10.1063/1.1744102

Cashman, K. V. (2020). Crystal size distribution (CSD) analysis of volcanic samples: Advances and challenges. *Frontiers of Earth Science*, *8*. https://doi.org/10.3389/feart.2020.00291

Chen, L.-Q. (2002). Phase-field models for microstructure evolution. *Annual Review of Materials Research*, *32*(1), 113–140. https://doi.org/10.1146/annurev.matsci.32.112001.132041

Connolly, J. A. D., & Petrini, K. (2002). An automated strategy for calculation of phase diagram sections and retrieval of rock properties as a function of physical conditions. *Journal of Metamorphic Geology*, *20*(7), 697–708. https://doi.org/10.1046/j.1525-1314.2002.00398.x

Cooper, R., & Kohlstedt, D. (1982). Interfacial energies in the olivine basalt system. In book: High pressure research in geophysics, 217–228.

de Leeuw, N. H., Parker, S. C., Catlow, C. R. A., & Price, G. D. (2000). Modelling the effect of water on the surface structure and stability of forsterite. *Physics and Chemistry of Minerals*, *27*(5), 332–341. https://doi.org/10.1007/s002690050262

Dingwell, D. (2006). Transport properties of magmas: Diffusion and rheology. *Elements*, *2*(5), 281–286. https://doi.org/10.2113/gselements.2.5.281

Eiken, J., Böttger, B., & Steinbach, I. (2006). Multiphase-field approach for multicomponent alloys with extrapolation scheme for numerical application. *Physical Review E - Statistical Physics, Plasmas, Fluids, and Related Interdisciplinary Topics*, *73*(6), 066122. https://doi.org/10.1103/PhysRevE.73.066122

Ford, C. E., Russell, D. G., Craven, J. A., & Fisk, M. R. (1983). Olivine-liquid equilibria: Temperature, pressure and composition dependence of the crystal/liquid cation partition coefficients for Mg, Fe2+, Ca and Mn. *Journal of Petrology*, *24*(3), 256–266. https://doi.org/10.1093/petrology/24.3.256

Ghiorso, M. S., & Sack, R. O. (1995). Chemical mass transfer in magmatic processes IV. A revised and internally consistent thermodynamic model for the interpolation and extrapolation of liquid-solid equilibria in magmatic systems at elevated temperatures and pressures. *Contributions to Mineralogy and Petrology*, *119*(2–3), 197–212. https://doi.org/10.1007/BF00307281

Ginzburg, V. L., & Landau, L. D. (1950). To the theory of superconductivity. *Zhurnal Eksperimental'noi i Teoreticheskoi Fiziki*, (20), 1064.

Grose, C. J., & Asimow, P. D. (2022). A multi-phase field model for mesoscopic interface dynamics with large bulk driving forces. *Computational Materials Science*, *212*, 111570. https://doi.org/10.1016/j.commatsci.2022.111570

Hersum, T., & Marsh, B. (2006). Igneous microstructures from kinetic models of crystallization. *Journal of Volcanology and Geothermal Research*, *154*(1–2), 34–47. https://doi.org/10.1016/j.jvolgeores.2005.09.018

Hersum, T., & Marsh, B. (2007). Igneous textures: On the kinetics behind the words. *Elements*, *3*(4), 247–252. https://doi.org/10.2113/gselements.3.4.247

Higgins, M. (2000). Measurement of crystal size distributions. *American Mineralogist*, *85*(9), 1105–1116. https://doi.org/10.2138/am-2000-8-901

Higgins, M. (2006). Verification of ideal semi-logarithmic, lognormal or fractal crystal size distributions from 2d datasets. *Journal of Volcanology and Geothermal Research*, *154*(1–2), 8–16. https://doi.org/10.1016/j.jvolgeores.2005.09.015

Holland, T. J. B., & Powell, R. (1998). An internally consistent thermodynamic data set for phases of petrological interest. *Journal of Metamorphic Geology*, *16*(3), 309–343. https://doi.org/10.1111/j.1525-1314.1998.00140.x

Karma, A. (2001). Phase-field formulation for quantitative modeling of alloy solidification. *Physical Review Letters*, *87*(11), 115701. https://doi.org/10.1103/PhysRevLett.87.115701

Karma, A., & Rappel, W.-J. (1998). Quantitative phase-field modeling of dendritic growth in two and three dimensions. *Physical Review E - Statistical Physics, Plasmas, Fluids, and Related Interdisciplinary Topics*, *57*(4), 4323–4349. https://doi.org/10.1103/PhysRevE.57.4323

Kim, H.-K., Ko, W.-S., Lee, H.-J., Kim, S., & Lee, B.-J. (2011). An identification scheme of grain boundaries and construction of a grain boundary energy database. *Scripta Materialia*, *64*(12), 1152–1155. https://doi.org/10.1016/j.scriptamat.2011.03.020

Kobayashi, R. (1993). Modeling and numerical simulations of dendritic crystal growth. *Physica D: Nonlinear Phenomena*, *63*(3), 410–423. https://doi.org/10.1016/0167-2789(93)90120-P

Kundin, J., Mushongera, L., & Emmerich, H. (2015). Phase-field modeling of microstructure formation during rapid solidification in inconel 718 superalloy. *Acta Materialia*, *95*, 343–356. https://doi.org/10.1016/j.actamat.2015.05.052

Kundin, J., & Steinbach, I. (2019). Comparative study of different anisotropy and potential formulations of phase-field models for dendritic solidification. *Computational Materials Science*, *170*, 109197. https://doi.org/10.1016/j.commatsci.2019.109197

Langer, J. S. (2021). Unpublished research notes 1978, as cited in: Progress in modelling solidification microstructures in metals and alloys: Dendrites and cells from 1700 to 2000. *International Materials Reviews*, *64*(6).

Lee, B.-J., & Choi, S.-H. (2004). Computation of grain boundary energies. *Modelling and Simulation in Materials Science and Engineering*, *12*(4), 621–632. https://doi.org/10.1088/0965-0393/12/4/005

Lilova, K., DeAngelis, M. T., Anovitz, L. M., & Navrotsky, A. (2018). Surface energy of fayalite and its effect on fe-si-o oxygen buffers and the olivine-spinel transition. *American Mineralogist*, *103*(10), 1599–1603. https://doi.org/10.2138/am-2018-6531

Lukas, H., Fries, S. G., & Sundman, B. (2007). *Computational thermodynamics: The Calphad method* (1st ed.). Cambridge University Press.

Marquardt, K., Rohrer, G., Morales, L., Rybacki, E., Marquardt, H., & Lin, B. (2015). The most frequent interfaces in olivine aggregates: The GBCD and its importance for grain boundary related processes. *Contributions to Mineralogy and Petrology*, *170*(4), 40. https://doi.org/10.1007/s00410-015-1193-9

Marsh, B. D. (1988). Crystal size distribution (CSD) in rocks and the kinetics and dynamics of crystallization. *Contributions to Mineralogy and Petrology*, *99*(3), 277–291. https://doi.org/10.1007/bf00375362

McFadden, G. B., Wheeler, A. A., Braun, R. J., Coriell, S. R., & Sekerka, R. F. (1993). Phase-field models for anisotropic interfaces. *Physical Review E - Statistical Physics, Plasmas, Fluids, and Related Interdisciplinary Topics*, *48*(3), 2016–2024. https://doi.org/10.1103/PhysRevE.48.2016

Miura, H. (2018). Phase-field model for growth and dissolution of a stoichiometric compound in a binary liquid. *Physical Review E - Statistical Physics, Plasmas, Fluids, and Related Interdisciplinary Topics*, *98*(2), 023311. https://doi.org/10.1103/PhysRevE.98.023311

Miura, H., Yokoyama, E., Nagashima, K., Tsukamoto, K., & Srivastava, A. (2010). Phase-field simulation for crystallization of a highly supercooled forsterite-chondrule melt droplet. *Journal of Applied Physics*, *108*(11), 114912. https://doi.org/10.1063/1.3504655

Morse, S. A., Davidson, J. P., Tepley, I., & Frank, J. (2017). Plagioclase zonation: An archive of trapped liquid and crustal contamination. *Elements*, *13*(6), 403–408. https://doi.org/10.2138/gselements.13.6.403

OpenPhase (2023). The open source phase field simulation package [Software]. ICAMS, Department "Scale Bridging and Thermodynamic Simulation", Ruhr-Universtuy Bochum. Retrieved from http://www.openphase.de/

Philpotts, A. R. (1988). *Petrography of igneous and metamorphic rocks* (1st ed.). Pearson.

Salama, H., Kundin, J., Shchyglo, O., Mohles, V., Marquardt, K., & Steinbach, I. (2020). Role of inclination dependence of grain boundary energy on the microstructure evolution during grain growth. *Acta Materialia*, *188*, 641–651. https://doi.org/10.1016/j.actamat.2020.02.043

Saylor, D., Mason, D., & Rohrer, G. (2000). Experimental method for determining surface energy anisotropy and its application to magnesia. *Journal of the American Ceramic Society*, *83*(5), 1226–1232. https://doi.org/10.1111/j.1151-2916.2000.tb01358.x

Spillar, V., & Dolejs, D. (2015). Heterogeneous nucleation as the predominant mode of crystallization in natural magmas: Numerical model and implications for crystal–melt interaction. *Contributions to Mineralogy and Petrology*, *169*(1), 4. https://doi.org/10.1007/s00410-014-1103-6

Spruzeniece, L., Späth, M., Urai, J. L., Ukar, E., Selzer, M., & Nestler, B. (2021). Wide-blocky veins explained by dependency of crystal growth rate on fracture surface type: Insights from phase-field modeling. *Geology*, *49*(6), 641–646. https://doi.org/10.1130/G48472.1

Steinbach, I. (2009). Phase-field models in materials science. *Modelling and Simulation in Materials Science and Engineering*, *17*(7), 073001. https://doi.org/10.1088/0965-0393/17/7/073001

Steinbach, I., Boettger, B., Eiken, J., Warnken, N., & Fries, S. G. (2007). CALPHAD and phase-field modeling: A successful liaison. *Journal of Phase Equilibria and Diffusion*, *28*(1), 101–106. https://doi.org/10.1007/s11669-006-9009-2

Steinbach, I., & Pezzolla, F. (1999). A generalized field method for multiphase transformations using interface fields. *Physica D*, *134*(4), 385–393. https://doi.org/10.1016/s0167-2789(99)00129-3

Taniguchi, H. (1988). Surface tension of melts in the system CaMgSi2O6-CaAl2Si2O8 and its structural significance. *Contributions to Mineralogy and Petrology*, *100*(4), 484–489. https://doi.org/10.1007/BF00371377

Welsch, B., Faure, F., Famin, V., Baronnet, A., & Bachèlery, P. (2012). Dendritic crystallization: A single process for all the textures of olivine in basalts. *Journal of Petrology*, *54*(3), 539–574. https://doi.org/10.1093/petrology/egs077

Wendler, F., Okamoto, A., & Blum, P. (2016). Phase-field modeling of epitaxial growth of polycrystalline quartz veins in hydrothermal experiments. *Geofluids*, *16*(2), 211–230. https://doi.org/10.1111/gfl.12144

Wieser, P. E., Edmonds, M., Maclennan, J., & Wheeler, J. (2020). Microstructural constraints on magmatic mushes under Kilauea volcano, Hawai'i. *Nature Communications*, *11*(1), 14. https://doi.org/10.1038/s41467-019-13635-y

Wieser, P. E., Vukmanovic, Z., Kilian, R., Ringe, E., Holness, M. B., Maclennan, J., & Edmonds, M. (2019). To sink, swim, twin, or nucleate: A critical appraisal of crystal aggregation processes. *Geology*, *47*(10), 948–952. https://doi.org/10.1130/G46660.1

Zieg, M., & Lofgren, G. (2002). Experimental determination of olivine growth rates in chondrules. In *33rd annual lunar and planetary science conference, March 11–15*. abstract no.1373.